Adhesive Strength, Superhardness, and the Phase and Elemental Compositions of Nanostructured Coatings Based on Ti–Hf–Si–N

A. D. Pogrebnjak[a, b, *], V. M. Beresnev[c], A. A. Demianenko[a], V. S. Baidak[a], F. F. Komarov[d], M. V. Kaverin[a], N. A. Makhmudov[e], and D. A. Kolesnikov[f]

[a] *Sumy State University, Rymsky Korsakov 2 Str., Sumy, 40007 Ukraine*

[b] *Kurdyumov Institute for Metal Physics, National Academy of Sciences of Ukraine, bulv. Akademika Vernadskogo 36, Kyiv, 03680 Ukraine*

* *e-mail: alexp@i.ua*

[c] *Karazin Kharkiv National University, pl. Svobody 4, Kharkiv, 61022 Ukraine*

[d] *Belarusian State University, pr. Nezavisimosti 4, Minsk, 220030 Belarus*

[e] *Samarkand Branch of the Tashkent University of Information Technology, ul. Shokhrukh Mirzo 47a, Samarkand, Uzbekistan*

[f] *Belgorod State University, ul. Pobedy 85, Belgorod, 308015 Russia*

Abstract—New superhard coatings based on Ti–Hf–Si–N with good physical and mechanical properties have been fabricated. A comparative analysis of the physical, mechanical, and tribomechanical characteristics of the coatings has been performed. The values of hardness, modulus of elasticity, elastic recovery, adhesive strength, friction coefficient, and wear rate of the coatings have been determined and calculated. The specific features of deformation and fracture of the coatings deposited on a steel substrate during the adhesion tests have been described. It has been shown that the parameters measured during scratching make it possible to distinguish the threshold values of the critical load, which lead to different (cohesive and adhesive) types of failure of the coatings during tribological tests. The stoichiometry for different series of samples with Ti–Hf–Si–N coatings has been determined using Rutherford backscattering, secondary ion mass spectrometry, and energy dispersive microanalysis.

1. INTRODUCTION

An important problem of modern materials science is the development of new properties of coatings and multicomponent solid nanostructures (nanocomposite coatings), for example, based on the Zr–Ti–Si–N, Zr–Ti–N, and Mo–Si–N solid solutions with a high hardness (more than 40 GPa) and a high thermal stability (above 1200°C) [1–4]. Multicomponent nanostructured coatings are of great interest owing to the unique properties inherent in nanoscale materials. Multifunctional thin-film materials on the surface of mechanical engineering products that operate under load should possess high adhesive and fatigue strengths, low friction coefficient, high durability, and high corrosion resistance. At the same time, the problem of development of new coatings is put forward taking into account the fact that the temperature of deposition of coatings (films) should reach 550–600°C. The compliance with this requirement makes it possible to complete the process of spinodal segregation at the grain boundaries. It is also known that the actual hardness of these coatings can be as high as 80 GPa and above when nanograins consisting of *nc*-TiN or *nc*-(Zr,Ti)N are covered with one or several layers of amorphous or quasi-amorphous α-Si_3N_4, BN, and others. An analysis of the available experimental results has demonstrated that an important role in solid materials is played not only by the grain size but also by the structural state of interfaces (grain boundaries). Since the amount of atoms located at grain boundaries in nanocrystals reaches 30–50%, the properties of the material substantially depend on the state of grain boundaries, or, more precisely, on the width of the near-boundary region in which, for example, the lattice parameter deviates from the standard value, as well as on the misorientation of grains and boundaries, the degree of imperfection of boundaries, and the free volume. Nanocrystalline materials, which, in addition to nanoscale crystallites, contain extended interfaces with a partially disordered structure, exhibit new properties as compared to coarse-grained materials of the same composition. Therefore, the development of new coatings with high hardness (superhardness of higher than 40 GPa), high modulus

Parameters of the Ti–Hf–Si–N films and the conditions of their deposition for different series of samples

Sample series no.	Mode	Lattice parameter, nm	Average crystallite size, nm	Hf content in the (Hf,Ti) solid solution***, at %	Hardness, GPa	Nitrogen pressure in the chamber, Pa	Potential at the substrate, V
23	Separated	0.4294*	6.7**	19	42.7	0.7	–100
28	Straight-flow	0.4430	4.0	65	37.4	0.6–0.7	–200
35	The same	0.4437	4.3	69	38.3	0.6–0.7	–100
37	Separated	0.4337	5.0	33	48.6	0.6	–200
31	The same	0.4370	3.9	45	39.7	0.3	–200

* In textured crystallites of the samples of series no. 23 with the ⟨220⟩ texture axis, the lattice parameter is larger than 0.43602 nm, which can be associated with the higher Hf content (approximately 40 at %) in the samples.

** In the direction of the texture axis of the crystallites, the average crystallite size is larger and equal to 10.6 nm.

*** The calculation was performed according to the Vegard's rule using the lattice parameter of the solid solution (the influence of macrostresses on the shift of the diffraction lines was disregarded).

of elasticity, and high thermal stability (at temperatures above 1200°C), as well as with the properties that remain unchanged during the service life, is an important problem. The purpose of this work is to design and fabricate a new type of Ti–Hf–Si–N-based superhard nanostructured coatings and to investigate their properties and structure with variations in the preparation conditions.

Quantitative measurements and interpretation of the properties of nanostructured coatings require the use of new certified methods for analyzing surface layers at the submicrometer and nanometer levels. Investigation of the deformation characteristics in the process of continuous pressing of an indenter has been widely developed in recent years owing to the use of the nanoindentation method (for the coatings ISO/CD 14577-4 [5]) under small loads, which has made it possible to determine the hardness, the modulus of elasticity, and the elastic recovery of coatings [6, 7]. Therefore, in this study, particular attention has been focused on the determination of the adhesive strength and measurements of the deformation characteristics of coatings in the Ti–Hf–Si–N/substrate system during the standard adhesion (standard ISO/DIS 20502) and tribological (ISO 20808) tests.

2. EXPERIMENTAL SETUP AND MEASUREMENT TECHNIQUE

Films of the Ti–Hf–Si–N composition were deposited on steel 3 substrates (20 mm in diameter and 3 mm in thickness) in a vacuum chamber with the use of a vacuum source in the high-frequency (HF) discharge of the sintered Ti–Hf–Si cathode. In order to synthesize nitrides, the accelerator chamber was filled with atomic nitrogen at different pressures and potentials applied to the substrate. The deposition parameters are presented in the table. The deposition of the films was carried out using a "Bulat-3T" vacuum-arc source with an HF generator [8, 9]. The bias potential was applied to the substrate from the HF generator in the form of pulses of damped oscillations with a frequency $f \leq 1$ MHz. The duration of each pulse was 60 μs, and the pulse repetition rate was ~10 kHz. The magnitude of the negative self-bias potential at the substrate due to the HF diode effect varied in the range 2–3 kV.

The prepared (deposited) coatings differed from each other primarily by the ratios of the atomic concentrations Ti/Hf. In the first series of samples, this ratio corresponded to $Ti_{54}Hf_{46}$, whereas the difference between the atomic concentrations in the second series of samples was larger and corresponded to $Ti_{64}Hf_{36}$. In this case, the silicon concentration varied insignificantly (in the range from 7.5 to 9.5 at %), as well as the nitrogen concentration, which varied in the range from 40 to 47 at %. All the other series of samples differed in concentration (composition) only slightly, but the phase composition (the ratio of the phases), the texture, and the substitution of Hf ions (atoms) in the Ti sites differed significantly. For example, the concentration of Hf atoms in the (Hf,Ti)N solid solution varied from 18 to 34 at %. It can be argued that these changes were associated with an increase in the absolute value of the bias potential applied to the substrate (from 0 to –200 V) and with a variation in the pressure in the accelerator chamber (from 0 to 0.7 Pa).

The elemental composition was investigated using secondary ion mass spectrometry (SIMS) on SAJW-0.5 mass spectrometers with quadrupole mass analyzers QMA-410 Balzers and SAWJ-01 GP-MS with glow discharge and a quadruple mass analyzer SRS-300 (Warsaw, Poland). A more complete information on the elemental composition of the coatings was obtained using the scheme of Rutherford backscattering (RBS) by He^+ ions with an energy of 1.3 MeV (the scattering angle was 170°; at normal incidence of the probing ions on the samples, the energy resolution of

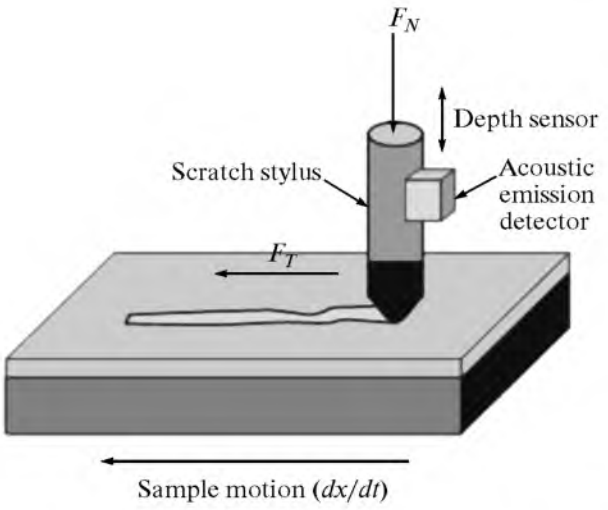

Fig. 1. Experimental setup for the determination of the adhesive/cohesive strength. Designations: F_N is the normal load, and F_T is the friction force.

the detector was 16 keV). The dose of helium ions was 5 μCi. The RBS spectra were processed with the standard (international) program for obtaining the in-depth concentration distribution profiles of elements [10].

The mechanical properties of the coatings were investigated by the nanoindentation method using a Nanoindenter G200 (MES Systems, United States) with a Berkovich three-sided diamond pyramid with a radius of curvature at the apex of approximately 20 nm [11]. The accuracy in the measurement of the indentation depth was ±0.04 nm. In order to decrease the influence of the substrate on the results of the nanohardness measurements, the nanoindentation of the samples with coatings was performed down to a depth of 200 nm. In this case, the imprints were made at a distance of 15 μm from each other. For each sample, we carried out at least five measurements using the continuous stiffness measurement (CSM) technique. The penetration depth of the nanoindenter was substantially less than 0.1 of the coating (film) thickness [12]. The loading–unloading curves were analyzed using the Oliver–Pharr method.

The X-ray diffraction analysis of the nanostructured films was performed on two diffractometers: a DRON-4 diffractometer (St. Petersburg, Russia) and an X'Pert PANalitical diffractometer (Netherlands) (scan step, 0.05°; scan speed, 0.05°; $U = 40$ kV; $I = 40$ mA; copper cathode).

The cross sections of the coating–substrate system were prepared using an ion beam. Then, these cross sections were used to analyze the morphology, structure, and elemental composition of the system. Friction tests were carried out on a TAU-1M tribometer under dry friction conditions. The friction coefficient and wear resistance of the coatings were determined in the course of the back-and-forth sliding at room temperature (22 ± 1°C) and a relative humidity of 80 ± 5%. The speed of movement of the table with the sample was 4 mm/s. The rounded indenter with a radius of curvature of 0.5 mm was fabricated from the VK8 hard alloy. The load on the indenter in the tests was 1 N.

In order to determine the adhesive/cohesive strength and the resistance to scratching, as well as to investigate the fracture mechanism, we used a REVETEST scratch tester (CSM Instruments) [13] (Fig. 1). On the surface of the coating under a continuously increasing load, scratches were made with a spherical indenter of the "Rockwell C" type with a radius of curvature of 200 μm. Simultaneously, we measured the acoustic emission power, the friction coefficient, the penetration depth of the indenter, and the normal load (F_N). In order to obtain reliable results, three scratches were made on the surface of each sample.

The tests were carried out under the following conditions: the load on the indenter was increased from 0.9 to 70.0 N, the speed of movement of the indenter was 1 mm/min, the scratch length was 10 mm, the loading rate was 6.91 N/min, the discrete signal frequency was 60 Hz, and the acoustic emission level was 9 Db.

In these tests, we determined the following minimum (critical) loads: L_{C1} corresponds to the beginning of the penetration of the indenter into the coating; L_{C2} corresponds to the beginning of the emergence of the first crack; L_{C3} corresponds to the peeling of some parts of the coating; and L_{C4} corresponds to the plastic wear of the coating down to the substrate. The measurements of a large number of different physical parameters in the process of testing favor an increase in the reliability of the methodology and the accuracy in the determination of the critical load. The deformation of the coatings with a diamond indenter was additionally examined using a built-in optical microscope and a Quanta 200 3D dual-beam scanning electron microscope equipped with a Pegasus 2000 integrated system for the microanalysis.

3. EXPERIMENTAL RESULTS AND DISCUSSION

Before proceeding to the analysis of the obtained X-ray diffraction data, it should be noted that, for a better understanding of the sequence of processes occurring during the deposition in the near-surface region, it is necessary to compare the heat of formation of the possible nitrides. According to [13], the standard heats of formation of such nitrides are as follows: $\Delta H298(\mathrm{HfN}) = -369.3$ kJ/mol, $\Delta H298(\mathrm{TiN}) = -336.6$ kJ/mol, and $\Delta H298(\mathrm{Si_3N_4}) = -738.1$ kJ/mol; i.e., the heats of formation for all the above systems are relatively large and negative. This indicates a rather

high probability of the formation of these systems at all stages of transfer of the material from the target to the substrate. Furthermore, the closeness of the values for the heats of formation of TiN and HfN creates conditions for the formation of a sufficiently homogeneous (Ti,Hf)N solid solution.

The X-ray diffraction investigations actually revealed the formation of just this system (since the diffraction peaks of the aforementioned phase are located between the peaks of the mononitrides TiN (JCPDS 38-1420) and HfN (JCPDS 33-0592), this phase has been identified by us as the substitutional solid solution (Ti,Hf)N), and the diffuse low-intensity peaks, which are observed in the X-ray diffraction pattern in the range of angles $2\theta = 40°–60°$, most likely, are attributed to the second phase α-Si_3N_4 phase (Fig. 2).

The analysis of the data obtained from the X-ray diffraction investigations has demonstrated that the coatings formed from the target of the same composition can have very different characteristic structural features depending on whether the beam is separated or non-separated. The results of this analysis are presented in the table.

It can be seen from Fig. 2 that the use of the direct-flow mode of plasma flow (without separation) leads to the formation of non-textured polycrystalline coatings with a sufficiently high relative intensity of the diffraction peaks (for comparable thicknesses of the coatings, the latter circumstance indicates that, in the solid solution, there is a relatively high concentration of hafnium with a higher reflectivity as compared to titanium).

In the case of the beam separation, the prepared (deposited) coatings are textured to different extents. When the low potential (~100 V) is applied to the substrate, it is the texture with the [110] axis. In this case, the structure of the coating consists of textured and non-textured crystallites. The volume content of textured crystallites accounts for approximately 40% of the total amount of crystallites in the coating, and the lattice parameter of the textured crystallites is increased as compared to that of the non-textured crystallites. This increase in the lattice parameter of the textured crystallites, most probably, can be caused by the inhomogeneous distribution of the hafnium atoms in the coating (these atoms are predominantly located in the lattice sites of the textured crystallites). The formation of the texture in this case leads to an increase in the average size of the crystallites in the direction of incidence of film-forming particles (i.e., in the direction perpendicular to the plane of the growing surface). For example, the average crystallite size in the fraction of non-textured crystallites is equal to 6.7 nm, whereas the average crystallite size in the fraction of textured crystallites is significantly larger and equal to 10.6 nm. This type of coatings is characterized by the highest nanohardness (see table).

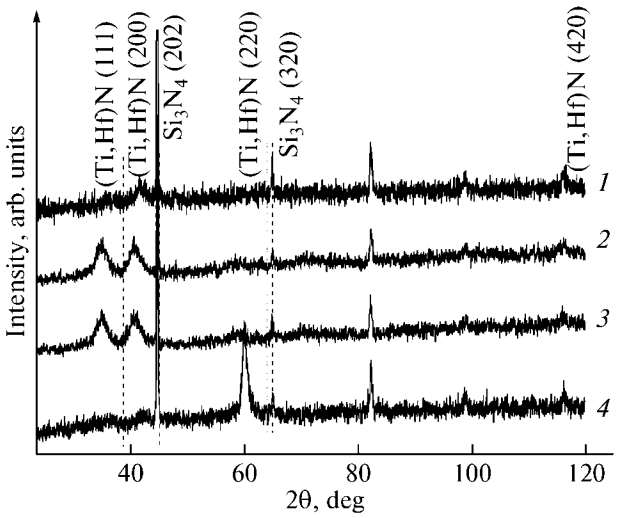

Fig. 2. X-ray diffraction patterns of the coatings deposited on a steel substrate at different potentials and in different modes: (*1*) −100 V, separated mode; (*2*) −200 V, direct-flow mode; (*3*) −100 V, direct-flow mode; and (*4*) −200 V, separated mode.

An increase in the voltage to −200 V and the use of the scheme with separation during the deposition lead to the formation of coatings with a smaller average size of crystallites (up to 5.0 nm), and the fraction of textured crystallites decreases significantly (their content becomes less than 20 vol %); the texture in this case has the [001] orientation. It should also be noted that an increase in the accelerating voltage from −100 to −200 V (i.e., an increase in the energy of the plasma flow) leads to the texturing of fractions and the formation of the lattice with the same value of the spatial period.

However, the lattice parameter in this case exceeds the lattice parameter of the non-textured fraction formed under the conditions where the low potential is applied to the substrate: it is equal to 0.4337 nm. According to the Vegard's rule for solid solutions, this value of the lattice parameter corresponds to the content of 33 at % Hf in the metal solid solution (Hf,Ti) of the nitride phase; in the calculations, we used the following tabulated values of the lattice parameters: 0.424173 nm for TiN (JCPDS 38-1420) and 0.452534 nm for HfN (JCPDS 33-0592).

As is known, compressive stresses generated in the coating lead to a decrease in the angle corresponding to the diffraction reflection observed in the X-ray diffraction pattern recorded in the θ–2θ scan mode; hence, the calculation leads to an overestimated value of the lattice parameter, i.e., to an overestimated value of the hafnium concentration in the solid solution (the error can reach 5–10 at %). Therefore, the results of the calculations performed in this work allowed us to judge only on the upper limit of the hafnium concentration in the solid solution.

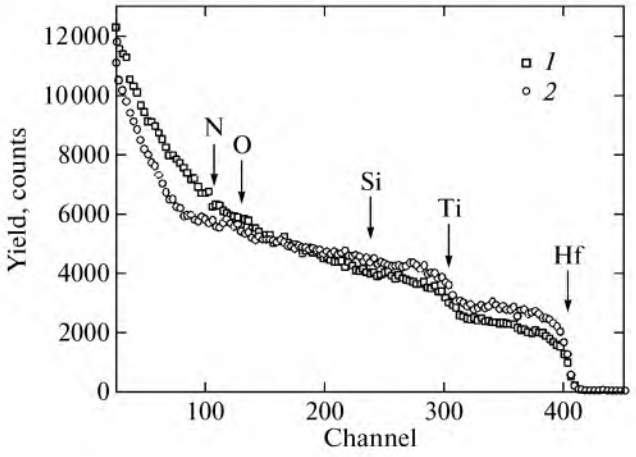

Fig. 3. Energy spectra of Rutherford backscattering of He^+ ions with an energy of 1.3 MeV for samples of the steel with the Ti–Hf–Si–N film: (*1*) at a potential of –100 V, $p = 0.6$ Pa (first series of samples), and (*2*) at a potential of –200 V, $p = 0.7$ Pa (second series of samples).

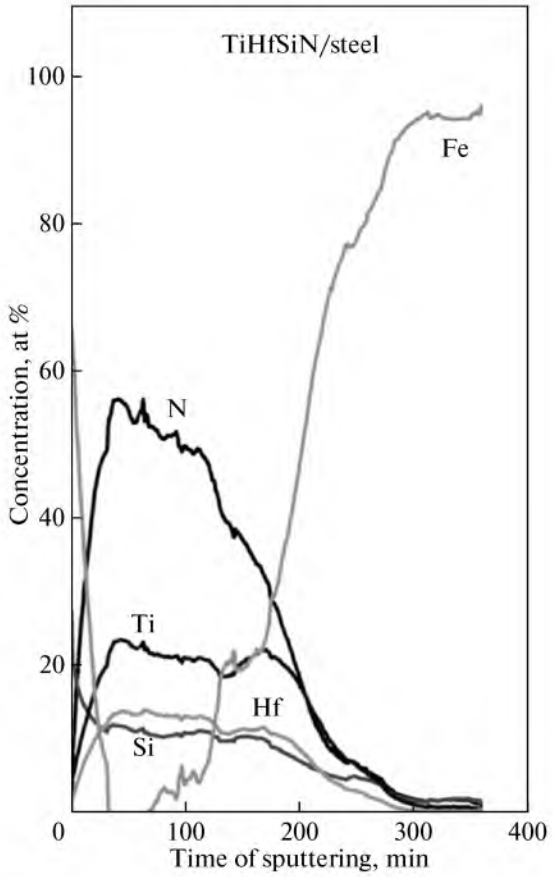

Fig. 4. Concentration profiles of elements in the Ti–Hf–Si–N film according to the SIMS analysis for the first series of samples. The high Fe concentration is observed in the substrate material (steel).

All the results presented above are related to the samples prepared at a characteristic pressure of 0.6–0.7 Pa in the working chamber during the deposition. In the case of a decrease in the pressure to 0.3 Pa, which we performed in the mode with separation at a voltage of –200 V (samples of series no. 31), the relative content of the heavier hafnium atoms in the coating decreases (see the lower row in the table). Furthermore, a decrease in the pressure leads to a decrease in the average size of the growing crystallites. The effects observed in this case can be due to an increase in the radiation factor as the pressure decreases. Indeed, a decrease in the pressure should be accompanied by a decrease in the probability of the energy loss by atoms during their collisions in the gap between the target and the substrate. Therefore, film-forming atoms with a relatively high energy during the deposition on the substrate can promote the processes of secondary sputtering and radiation-induced defect formation. As a result, this leads to an increase in the specific content of hafnium atoms in the coating in the first case and to an increase in the number of nuclei and, correspondingly, to a decrease in the average size of crystallites in the coating in the second case. In the coatings produced at a characteristic pressure of 0.6–0.7 Pa in the absence of beam separation (in the direct-flow mode), the lattice parameter has a higher value, which is determined by a higher concentration of hafnium atoms in these coatings (see table) [13]. Apparently, the more intensive deposition in the direct-flow mode leads to a decrease in the average size of the crystallites, which is caused by an increase in the intensity of nucleation per unit time. In addition, the more pronounced decrease in the average size of the crystallites is caused by the higher potential (–200 V) applied to the substrate. This is quite natural because the increase in the radiation factor leads to the dispersion of the structure [14]. Figure 3 presents the results obtained from the RBS investigation of the elemental composition of the superhard nanostructured Ti–Hf–Si–N films. It can be seen from this figure that, for the first series of samples with coatings (Fig. 3, curve *1*), the composition of the Ti–Hf–Si–N films is described by the formula $(Ti_{37}Hf_9Si_8)N_{46}$.

The concentration distribution profiles of elements over the depth of the Ti–Hf–Si–N coating, which correspond to the RBS spectra (Fig. 3), are calculated under the assumption that the atomic density of the layer is close to the atomic density of titanium nitride.

It is well known that Rutherford backscattering is a reference method for determining the concentration of elements with a large atomic number, as well as for determining the thickness of the films. Furthermore, it is a nondestructive method, and this property is its advantage. At the same time, secondary ion mass spectrometry is a more sensitive method of analysis (the detection limit is $\sim 10^{-6}$ at %) (Fig. 4). Therefore, a comparison of the results obtained using the RBS,

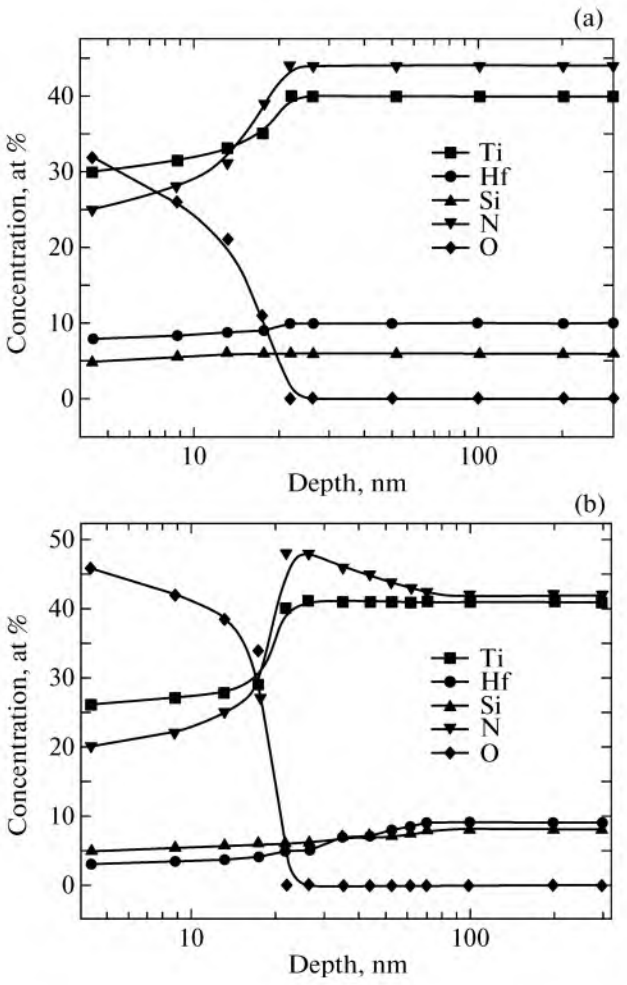

Fig. 5. (a) Concentration profiles of the elements involved in the coating composition according to the RBS data (including uncontrollable impurities). (b) Concentration distributions of elements over the depth of the Ti–Hf–Si–N coating according to the RBS data taking into account that the atomic density of the layer is close to the atomic density of titanium nitride.

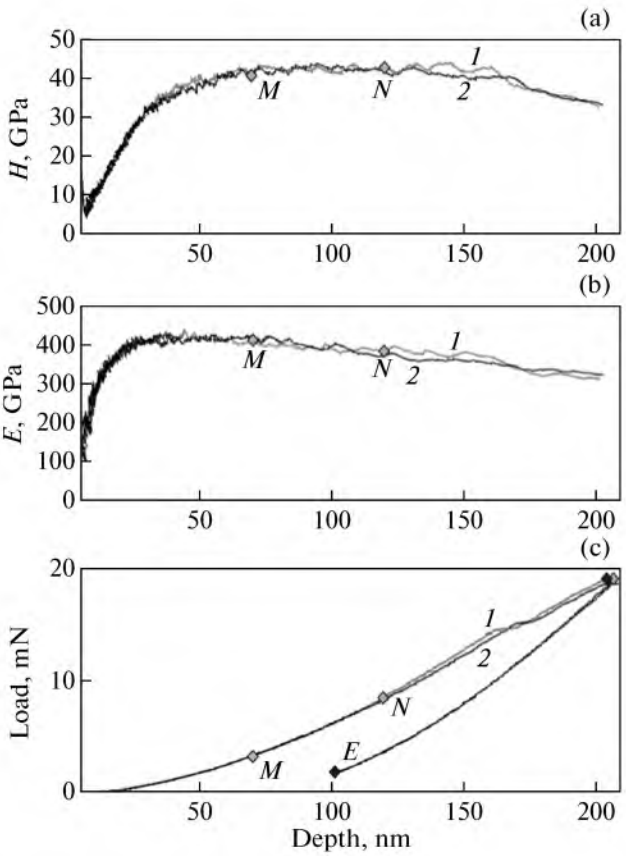

Fig. 6. Dependences of (a) the hardness H, (b) the modulus of elasticity E, and (c) the nanoindenter load on the indentation depth. Symbols indicate places where the values of H, E, and the load were measured. Curves *1* and *2* correspond to different measurements for the same sample. In panel (c), the gray and black symbols indicate places of measurements for curves *1* and *2*, respectively.

SIMS, and glow discharge mass spectrometry (GDMS) methods provides a more realistic picture of the distribution of the elemental composition of the coating over the depth of the layer. This has made it possible to analyze the composition of the film as a whole over the depth from the film surface to the film–substrate interface, including the determination of concentrations of oxygen and carbon uncontrollable impurities, which come from the residual atmosphere in the working chamber. Figures 5a and 5b show the in-depth concentration profiles of elements (including uncontrollable impurities) involved in the composition of the coating, which were obtained using the RBS method. These profiles were constructed without taking into account the results of the SIMS analysis. It can be seen from the results presented in these figures that, in the coating, oxygen exists only in the surface layer with a depth of 10–12 nm when the thickness of the coating exceeds a micrometer.

Thus, we obtained the stoichiometric composition $(Ti_{37}Hf_9Si_8)N_{46}$ for the first series of samples when the thickness of the coating (film) was equal to 1 ± 0.012 μm. By increasing the bias potential at the substrate to −200 V and changing the pressure in the working chamber from 0.3 to 0.7 Pa, we obtained the second series of samples with the Ti–Hf–Si–N films.

The composition of the films in the second series of samples was investigated using the RBS method (curve *2* in Fig. 3) and then was compared with the results obtained from the energy dispersive X-ray spectroscopy and SIMS analyses. As a result, we obtained the following stoichiometry of the films: $(Ti_{28}Hf_{18}Si_9)N_{45}$. From the nanohardness measurements carried out with the use of a Berkovich three-sided diamond pyramid [1], we determined the nanohardness $H = 42.7$ GPa (Fig. 6a) and the modulus of elasticity $E = 390 \pm 17$ GPa (Fig. 6b) for the first series of samples and the nanohardness $H = 48.4 \pm 1.4$ GPa

and the modulus of elasticity $E = 520 \pm 12$ GPa for the second series of samples with the Ti–Hf–Si–N films. The places where these values were measured are marked by symbols on the dependences of the nanohardness H and the modulus of elasticity E on the indentation depth (Figs. 6a, 6b). The phase composition of the coatings was investigated using the X-ray powder diffraction analysis and calculations of the lattice parameters. These investigations revealed that a two-phase system consisting of the substitutional solid solution (Ti,Hf)N and the α-Si_3N_4 phase is formed in the coating. The dependences of the nanoindenter load on the nanoindentation depth are shown in Fig. 6c.

It was also found that the lattice parameter of the solid solution decreases with an increase in the pressure in the working chamber and does not depend on the potential applied to the substrate (see table). For samples of series no. 23, we revealed that the (Ti,Hf)N solid solution has the smallest value of the lattice parameter among all those observed in our study.

The calculation of the sizes of nanograins from the Debye–Scherrer formula demonstrated that, for the second series of samples with coatings of the $(Ti_{28}Hf_{18}Si_9)N_{45}$ composition, the grain size is approximately 1.5 times smaller than that for the first series of samples, namely, it is equal to 4 nm. The size of the amorphous (or quasi-amorphous) interlayer also turned out to be smaller than that for the first series of samples. Another possible explanation for the increase in the hardness of coatings can be associated with the decrease in the concentration of hafnium in the solid solution (Ti,Hf)N, as well as with the change in the thickness of the amorphous (quasi-amorphous) interlayer of the α-Si_3N_4 phase; furthermore, the latter explanation is preferable.

The analysis of the preliminary results obtained using high-resolution transmission electron microscopy with diffraction by samples with superhard nanostructured films revealed that the size of nanograined phases *nc*-(Ti,Hf) is consistent in the order of magnitude with the results of the X-ray diffraction analysis (2–5 nm) and that the thickness of the α-Si_3N_4 interlayer covering the (Ti,Hf)N nanograins lies in the range 0.8–1.8 nm.

It is known that nanocomposites with a hardness higher than 40 GPa are frequently referred to as superhard materials [1–3], whereas those with a hardness of 80 GPa and higher are referred to as ultrahard materials. In this work, we fabricated coatings with a hardness in the range from 42.7 to 48.4 ± 1.4 GPa; therefore, they are superhard.

For the Ti–Hf–Si–N coatings fabricated in the first series of samples, the hardness and the modulus of elasticity remained unchanged during the long-term storage (from 6 to 12 months). We did not analyze their thermal stability and resistance to oxidation. However, since the temperature of the substrate during deposition of the films does not exceed 350–400°C, which is considerably below the temperature of complete phase segregation at the grain boundaries (550–620°C) [1, 4, 9], we cannot argue that the process of spinodal segregation at the nanograin boundaries in the system under investigation is completely finished.

For the sample of series no. 35, we found that the coefficient of friction at the initial stage is equal to 0.12, which, most likely, indicates the smallest surface roughness of this coating as compared to other coatings investigated in this work.

At the next stage, after the wear of a 2.5-m-long segment, the coating undergoes a fracture (with the formation of hollows and cracks), i.e., an abrasive wear. As a result, the friction coefficient increases to 0.45 (which corresponds to the moderate hardness of the coating $H = 38.3$ GPa, but, quite possibly, can be associated with the presence of a quasi-amorphous binder (Si_3N_4) and with a lower concentration of hafnium atoms in the (TiHf)N solid solution).

At the stage of the removal of roughnesses for the sample of series no. 23, the friction coefficient increases to 0.25; then, at the stage of the steady-state wear, it becomes equal to 0.20, which gives grounds to argue that this coating is the hardest.

A detailed investigation of the parameters such as the friction coefficient, the acoustic emission, and the penetration depth of the indenter was carried out for all samples.

The results of tests on the sample of series no. 23 with the use of the REVETEST scratch tester are presented in Fig. 7a.

It should be noted that, as the load on the indenter increases, the dependence of the friction coefficient on the load becomes oscillatory in character: an increase in the friction coefficient is accompanied by a sudden burst of acoustic emission and a retardation of penetration of the indenter into the material. This behavior of all the measured parameters indicates that the hard coating with a thickness of larger than 1 μm on the surface of a softer material exhibits a significant resistance to the diamond indenter until it is completely abraded under large loads [11].

When testing the coating, we can clearly identified threshold values of the critical load, which lead to different types of fracture. The fracture of the coating begins with the emergence of individual chevron cracks at the bottom of the wear groove, which is responsible for the increase in local stresses and friction force. This leads to a rapid wear of the coating (Fig. 7b).

In this work, two main critical loads were determined from the changes in the curves of the dependences of the friction coefficient and acoustic emission on the scribing load (Fig. 7a). The first critical load corresponds to the onset of cohesive failure of the coating, whereas the second critical load corresponds

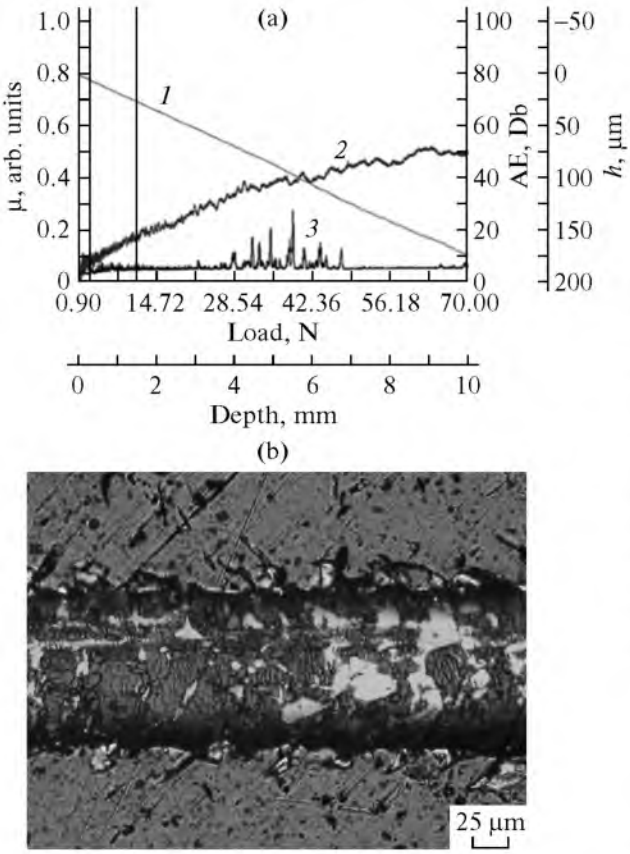

Fig. 7. Results of adhesion tests of the Ti–Hf–Si–N coating/steel substrate system for the sample of series no. 23: (a) (*1*) the penetration depth *h*, (*2*) the friction coefficient μ, and (*3*) the acoustic emission (AE) and (b) structure of the coating in the fracture zone at loads in the range 0.9–90.0 N.

to the plastic wear of the coating (adhesive failure). According to the results of adhesion tests, we can argue that the cohesive failure of the sample of series no. 23 occurs at a load of 2.38 N, and its adhesive failure, at a load of 9.81 N.

4. CONCLUSIONS

New superhard nanostructured coatings (films) based on Ti–Hf–Si–N with high physical and mechanical characteristics and different stoichiometries (depending on the deposition conditions) have been fabricated. It has been found that a decrease in the size of *nc*-(Ti,Hf)N nanograins from 6.7 to 5.0 nm and the formation of the α-Si_3N_4 phase (in the form of an amorphous or quasi-amorphous interlayer between the nanograins) result in an increase in the nanohardness from 42.7 to 48.4 ± 1.4 GPa. It has been established that, with an increase in the accelerating voltage to −200 V (separated and non-separated beams) during the deposition, the coatings with a smaller average crystallite size (up to 5.0 nm) are formed on the substrate. An increase in the accelerating voltage from −100 to −200 V leads to the same value of the lattice parameter for both the textured and non-textured factions. In the case where the pressure decreases to 0.3 Pa, the relative content of Hf atoms in the coating increases and the average size of growing crystallites decreases.

Thus, the adhesion and tribological tests have made it possible to determine the adhesive strength, friction coefficient, and deformation characteristics of the Ti–Hf–Si–N coatings on the steel substrate. Based on measurements of different physical parameters during the adhesion tests, the processes of elastic and plastic deformations in the coating/substrate system have been described, and the threshold values of the critical load leading to different (cohesive and adhesive) types of failure of the coatings have been determined. The synthesized coatings have high values of the hardness, wear resistance, and adhesion to the substrate and low values of the modulus of elasticity and friction coefficient, which makes them promising thin-film materials for the use in mechanical engineering.

ACKNOWLEDGMENTS

We would like to thank O.V. Sobol, P. Konarskii, and V.V. Uglov for their assistance in performing the experiments.

This study was supported by the State Foundation for Basic Research of Ukraine (project no. SFBRU F41.20-2011) and the Belarusian Republican Foundation for Fundamental Research (project no. BRFBR T11K-058).

REFERENCES

1. A. D. Pogrebnyak, O. V. Sobol', V. M. Beresnev, P. V. Turbin, S. N. Dub, G. V. Kirik, and A. E. Dmitrienko, Tech. Phys. Lett. **35** (10), 925 (2009).
2. A. D. Pogrebnjak, M. M. Danilionok, V. V. Uglov, N. K. Erdybaeva, G. V. Kirik, S. N. Dub, V. S. Rusakov, A. P. Shypylenko, P. V. Zukovski, and Yu. Zh. Tuleushev, Vacuum **83** (Suppl. 1), S235 (2009).
3. A. D. Pogrebnyak, A. P. Shipilenko, Yu. Zh. Tuleushev, M. M. Danilenok, A. A. Drobyshevskaya, V. M. Beresnev, N. K. Erdybaeva, and V. V. Uglov, Russ. Phys. J. **52** (12), 1317 (2009).
4. V. V. Uglov, V. M. Anischik, S. V. Zlotskij, G. Abadias, and S. N. Dub, Surf. Coat. Technol. **202**, 2394 (2008).
5. http://www.iso.org.
6. R. A. Andrievskii, G. V. Kalinnikov, N. Hellgren, P. Sandstrom, and D. V. Shtanskii, Phys. Solid State **42** (9), 1671 (2000).
7. R. A. Andrievskii and A. M. Glezer, Phys.—Usp. **52** (4), 315 (2009).

8. A. D. Pogrebnyak, A. P. Shpak, N. A. Azarenkov, and V. M. Beresnev, Phys.—Usp. **52** (1), 29 (2009).
9. R. F. Zhang, A. S. Argon, and S. Veprek, Phys. Rev. B: Condens. Matter **79**, 245426 (2009).
10. J. Musil, P. Baroch, and P. Zeman, in *Plasma Surface Engineering Research and Its Practical Applications*, Ed. by R. Wei (Research Signpost, Singapore, 2007), pp. 1–34.
11. R. F. Zhang, S. H. Sheng, and S. Veprek, Appl. Phys. Lett. **91**, 031906 (2007).
12. A. D. Pogrebnjak, M. Yu. Tashmetov, A. V. Pshyk, O. V. Sobol, V. M. Beresnev, P. V. Turbin, G. V. Kirik, and M. V. Kaverin, Ceram. Eng. Sci. Proc. **31** (7), 127 (2010).
13. *Smithells Metals Reference Book*, Ed. by W. F. Gale and T. C. Totemeier (Butterworth–Heinemann, Oxford, 1976; Metallurgiya, Moscow, 1980).
14. A. D. Korotaev, V. D. Borisov, V. Yu. Mashkov, S. V. Ovchinnikov, Yu. P. Pinzhin, and A. N. Tyumentsev, Fiz. Mezomekh. **12**, 79 (2009).